Implant Resonance and the Mechanostat Theory: Applications of Therapeutic Ultrasound for Porous Metallic Scaffolds

Joseph Deering[1*], Alexandre Presas[2], Bosco Yu[1], David Valentin[2], Christian Heiss[3,4], Wolfram A. Bosbach[3,4], Kathryn Grandfield[1,5*]

[1] Department of Materials Science and Engineering, McMaster University, Hamilton, ON, Canada

[2] Center for Industrial Diagnostics and Fluid Dynamics (CDIF), Polytechnic University of Catalonia (UPC), Barcelona, Spain

[3] Experimental Trauma Surgery, Justus-Liebig-University of Giessen, Germany

[4] Department of Trauma, Hand, and Reconstructive Surgery, University Hospital of Giessen, Germany

[5] School of Biomedical Engineering, McMaster University, Hamilton, ON, Canada

[*] Corresponding authors:

|	
Joseph Deering	Prof. Kathryn Grandfield
McMaster University	McMaster University
1280 Main Street West	1280 Main Street West
Hamilton, ON, L8S 4L7	Hamilton, ON, L8S 4L7
Canada	Canada
Email: deeringj@mcmaster.ca	Email: kgrandfield@mcmaster.ca

Abstract

The development of treatment strategies for improving secondary stability at the bone-implant interface is a challenge. Porous implants are one solution for improving long-term implant stability, but the osteoconduction process of implants into the bone can be slow. Strain-driven osteogenesis from the mechanostat theory offers insight into pathways for post-operative treatment but mechanisms to deliver strain to the bone-implant interface need refinement. In this work, the use of therapeutic ultrasound is simulated to induce resonance into a porous implant structure. Local strains through the scaffold are measured by varying systemic variables such as damping ratio, applied vibrational force, primary bone-implant stability, and input frequency. At the natural frequency of the system with applied forces of 0.5 N and a damping ratio of 0.5%, roughly half of the nodes in the simulated environment exceed the microstrain threshold of 1000 $\mu\varepsilon$ required for new bone formation. A high degree of sensitivity was noted upon changing input frequency, with

minor sensitivities arising from damping ratio and applied vibrational force. These findings suggest that the application of therapeutic resonance to improve osseointegration of the bone-implant interface may be viable for applications including dental implants or segmental bone defects.

Keywords

Graphical abstract
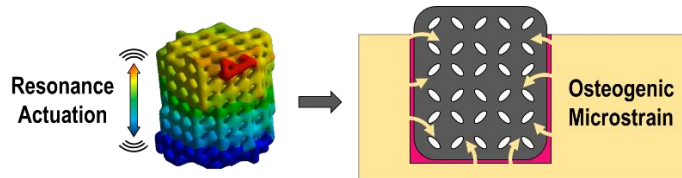
1   Introduction

Osseointegration at the implant interface is driven in part by the bulk properties and surface properties of the implant. Load sharing between traditional implant materials and the surrounding bone tissue can result in a phenomenon known as stress-shielding [1], where an increase in bone resorption is observed that is proportional to the stiffness mismatch between the implant and the surrounding bone tissue [2]. Stress shielding increases the likelihood of periprosthetic fracture as a result of these structural changes [3]. The intentional introduction of porosity into an implant can reduce the magnitude of the bone-implant stiffness mismatch [4], preventing long-term osteolysis and improving bone anchorage to the implant [5]. With advances in the field of additive manufacturing, these porous architectures can be fabricated with high precision and with complex repeating topologies [6].

An unsolved problem of implant technology is the loosening of implant-bone interfaces. It is known that optimised results can be achieved through implant geometry optimization. Geometric features can be classified by their size into micro, meso, and macro entities [7]. Optimization on the macroscale includes additional screws which fixate the acetabular component of a hip implant replacement in the pelvic bone. Spikes or bolts are equally used today. On the microscale, bioactive surface coatings [8–10] and microstructured surface patterns are an option [11] for both orthopaedic implants and dental implants.

The use of porous metallic implants is one option to better mechanical anchorage due to their osteoconductive nature [12]. It is important to develop scaffold designs which can be applied to a broad spectrum of implant sizes and topologies. Results from osseointegration depend on both the size of an inflicted bone defect, the specific animal model, and the bone structure [13]. Factors such as pore size and unit cell topography for a repeating porous structure have been shown to influence the corresponding mechanical properties of the implant [14–16] and the associated bone histomorphometry during implant removal [17]. For porous implants, it is important to consider all strategies to improve osteoconduction and secondary stability of the implant *in vivo*.

The application of ultrasound is one technique that has been historically used in biomedical applications to increase the activity of various stem cell lines [18–20], ablate neoplastic cells [21–23], or help treat biofilms [24,25]. Specific to *pseudarthrosis* in bone, the use of low-intensity pulsed

ultrasound (LIPUS) has been shown to possibly aid in bone regeneration and healing of non-unions [26,27], where LIPUS treatment may be effective for *de novo* bone formation during fracture healing [28,29] and maturation of existing bone [30,31] within a defect site. A broad range of pulsed frequencies that spans the kilohertz [32] and megahertz [33–35] scales have been shown to induce favourable conditions for osteogenesis. In particular, LIPUS specific to bone applications has been shown to upregulate alkaline phosphatase [36,37], osteocalcin [36–38], and members of the transformation growth factor β superfamily [39,40], among other growth factors.

De novo bone tissue is also sensitive to these types of mechanical factors, where bone structure is mediated by local microstrain within the defect site [41–43] and coordinated mechanosensation by osteocytes. Microstrain of 1000 µɛ and above have shown to be correlated to increase osteogenic activity [41,44]. Early work from Frost proposed minimum effective stresses for modeling and remodeling events in the mechanostat theory, where the onset of bone remodelling events can begin at strains as low as 50-200 µɛ and osteogenic modeling events are encouraged at higher strains [45,46]. While most of these seminal works focus on the application of cyclical bending loads to murine tibiae, these techniques cannot easily translate to clinical practices.

Instead, this study aims to simulate the application of osteogenic strains using therapeutic ultrasound for implant resonance. Where the potential for kHz-range resonance has been speculated to induce osteogenesis in porous constructs [32], the response of a given microenvironment in the porous structure has not been assessed in this type of resonance. Therefore, there is no standing clarity as to whether the osteogenic response is localized within the scaffold exterior, or if homogenous strain-dependent bone nucleation can occur deep within the interior of the metallic scaffold. In this work, the authors aim to define systemic variables that can affect the frequency-response of a porous metallic scaffold and qualify their respective importance for meeting osteogenic strain requirements. Herein, the authors investigate the effect of system damping ratio, applied force, input frequency and primary stability on the resulting strain distribution in the implant. The authors also show that some systemic variables influence the specific location within the implant interior where these osteogenic thresholds are exceeded. This offers new perspectives relating to the application of therapeutic ultrasound for improved osseointegration of metallic materials and frames some constraints for suitable biological applications.

2 Methods

2.1 Scaffold design and fabrication

Reticulated porous constructs were designed using Autodesk Netfabb. A cylindrical model with a radius of 4 mm and a height of 8.5 mm was rotated 45° about its X and Y axes before being populated with a repeating body-centred cubic (BCC) strut configuration and rotated back to its original orientation. Where the benchmark animal model for bone regeneration is the rabbit model, the large diameter of such an implant analogue is consistent with leporine calvarial defects and the extended implant length aids in examining the effect of the longer critical tibial/femoral defect. The unit cell size of the implant was defined at 1.200 mm with a strut thickness of 450 µm to produce the geometry pictured in Figure 1.
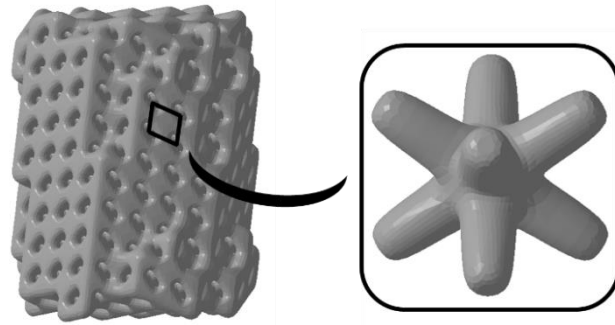
Figure 1 – Scaffold with reticulated body-centred cubic architecture for linear elastic measurements. Geometries were exported for vibrational analysis in Workbench 2020 R1 (ANSYS®) and fabricated with selective laser melting using 304L stainless steel powder. Struts are sized at 450 µm with a unit cell size of 1.2 mm.

Scaffolds were manufactured using gas atomized 304L stainless steel powder (Carpenter Technology Corporation) with a powder size distribution range of 15-45 µm. Specimens were fabricated using selective laser melting (EOSINT M280, EOS) with a 40 µm layer thickness, 80 µm hatch spacing, 800 mm/s scan speed, and 200 W laser power as described previously [32]. Samples for mechanical compression were printed with a 1 mm baseplate to improve part adhesion to the build plate. The baseplate was removed by electrical discharge machining.

Specimens were imaged via micro-computed tomography (Bruker Skyscan 1172) using a 100 kV beam and AlCu filter. The voxel size was set to 3.68 µm with a rotation step of 0.40°. Rotational images were converted to an image stack using NRecon (Bruker) with minor ring artifact and beam hardening corrections. The image stack was important to Dragonfly 4.1 (Object Research Systems) for extraction of a cylindrical sub-volume to assess part quality.

2.2 Response to mechanical compression

Porous constructs were subjected to mechanical compression on an Instron test frame at a deformation rate of 0.8 mm/min using a load-unload-reload procedure, where loading was applied parallel to the central axis of the cylinder. The porous scaffold was loaded to a force of 5.5 kN before being unloaded to a force of 1 kN. The samples were then loaded to 32 kN, a force beyond their yield point. Stresses were calculated assuming a full-density cross-section in the scaffold. The scaffold stiffness was measured in the region of unloading to account for settling effects. Compression of the porous specimens were conducted in triplicate. A solid cylinder of 304L stainless steel (H = 8.5 mm, R = 4 mm) was also compressed to calibrate for machine compliance and platen deformation (Supplemental S.1) in tests of the porous scaffolds. The solid cylinder for calibration was loaded to 12 kN, unloaded to 1 kN and reloaded to 32 kN where stiffness measurements were extracted in the region of unloading. A video outlining macroscale deformation during experimental compression can be found in Video S1, where images were recorded every 5 s.

2.3 Local linear elastic strains in compression

The same scaffold geometry was subjected to simulated compression. Using ANSYS Workbench 2020, R1® the model was meshed using 105,873 independent elements and 207,257 nodes. Elements were set to patch-forming tetrahedra, with an average volume of 0.0023 mm³ and average

surface area of 0.0360 mm². For the sensitivity analysis of the mesh, the values of the natural frequencies were considered. For a finer mesh, the obtained value for the first resonant frequency did not significantly change (less than 1% difference).

To simulate compressive loading for an implant with high primary stability, the bottom surface was considered to be clamped (i.e. nodes with zero displacement) and the same distributed force was applied on the upper surface (12 kN). This simulation considered a perfect linear elastic behaviour of the structure and the resulting strain is therefore proportional to the applied force. The elastic modulus during simulated compression was calibrated using the iteratively measured modulus of unloading from experimental compression tests. The locations of peak nodal strain through the scaffold under simulated loading were observed for both the entire scaffold and across the longitudinal midplane. Simulations of the strain distribution through the scaffold (Video S2) and through the scaffold midplane (Video S3) can be found in supplemental information.

2.4 Modal analysis

The resonant frequencies and mode shapes of the scaffold were determined with numerical modal analysis. Two different simulations were performed: one with the scaffold having free boundaries at either end and one with the bottom surface clamped. In this way, the basic differential equation (Eqn. 1) that governs the dynamic behaviour of an arbitrary structure was numerically solved.

(Eqn. 1) $$[M]\ddot{x} + [K]x = 0$$

Here, *[M]* is the matrix that contains the partial masses, *[K]* is the matrix containing element stiffnesses, and x is a vector containing element displacements. The eigenvalues of the harmonic solution $x = e^{j\omega t}$ are the natural frequencies and eigenvectors of the mode shapes. As in many cases, only the several first mode shapes were of relevant interest.

2.5 Local linear elastic strains in resonance

In order to determine, the strains in resonance, a harmonic analysis was performed. In this case the governing equation of the problem is as follows:

(Eqn. 2) $$[M]\ddot{x} + [C]\dot{x} + [K]x = F(t), \text{ with } F(t) = Fcos(\omega t)$$

F(t) is an oscillating distributed force on the upper surface and ω is the corresponding frequency. In case of resonance, ω_n is a natural frequency of the structure, determined by means of numerical modal analysis. The magnitude of the applied force is below 1.0 N, according to forces calculated in past studies [47]. The damping matrix *[C]* is defined by the damping ratio ε. Damping ratios of 0.3%, 0.5%, and 0.7% were adopted as possible values according to previous experimental studies of structures submerged in viscous fluids without mean velocity [47]. These values are within the range of metallic structures subjected to resonance by a piezoelectric patch [47]. For the bottom surface, two different boundary conditions were considered: clamped and free. The clamped condition is intended to simulate intimate bone-implant contact along the bottom surface of the implant while the free surface mimics weak primary implant stability. Once the element displacements (*x*) were obtained, the strains were generated by means of the material constitutive equations in ANSYS®.

Several simulations varying the magnitude of the applied force (0.3 N, 0.5 N, 0.7 N), input frequency (31.0 kHz, 39.4 kHz, and 42.0 kHz), and damping ratio (0.3%, 0.5%, and 0.7%) were performed. For the clamped case, two of these frequencies lie out of resonance on the frequency-response function (one below and one above the natural frequency) and the other lies in the resonant condition of the axial mode shape. For the free surface case, only the resonant condition of the axial mode shape was been simulated. An additional mode shape and stress distributions were mapped at 0.5 N and 0.5% for a clamped scaffold with a merged cylinder (h = 4 mm, Ø = 8 mm) at its base to assess the effect of modified implant geometry on local stress distributions.

3 Results and discussion

3.1 The occlusion-free structure of porous metallic implants

Micro-computed tomography reconstructions of the selective laser melted stainless steel scaffolds are shown in Figure 2. The cylindrical sub-volume shows the interior portion of the porous scaffold, where the pore space is represented by the darker regions and the metallic struts are represented as brighter regions. The interior pore network appears continuous through the scaffold, consistent with the high-tolerance capabilities afforded by the selective laser melting process [48]. Due to the offset orientation of the repeating unit cell, the pore architecture is offset from the z-axis of the build by 45°, as shown in the side profile of the sub-volume. From the top profile of the scaffold, this misorientation angle results in pores that are oblong in the cross-section. Within the sub-volume, distinct pores are visibly connected without substantial deformation or blockage. This is important to allow for osteoblast migration through the porous interior, especially since smaller pore sizes are prone to pore occlusion with anchored osteoblasts in the early stages of osseointegration [49].

Figure 2: Cylindrical volume (h = 7 mm, ∅ = 8 mm) extracted from the micro-CT reconstruction of an as-fabricated stainless steel scaffold. Pores (darker regions) in the stainless steel (lighter regions) appear ellipsoidal in cross-section as a result of the 45° unit cell tilt. Junctions between these pores are visible around the periphery of the cylindrical volume.

3.2 The mechanical properties of metallic scaffolds can mimic cortical bone

The bulk stress-strain relationship for porous stainless steel scaffolds can be found in Figure 3, where a video showing deformation over time can be found in Video S1. The simplified progression for compression of cellular solids consists of an initial linear elastic portion followed by a period of deformation and subsequent densification [50]. The plot from the porous cylinder shows consistency with the first two stages but lacks the eventual stiffness increase associated with significant densification. Comparing the shape of the BCC unit cell with known geometries that have stretch-dominated behaviour (by satisfying Maxwell's criterion) [51], this type of topology has a more efficient strength-to-weight ratio than comparably porous bend-dominated structures [51].

The modulus during unloading was measured to be 17.4 GPa ± 0.6 GPa, a 91% reduction in stiffness, where the onset of stiffening occurs at roughly 250 MPa in the steel scaffolds. This modulus value corresponds to at least a tenfold stiffness reduction compared to full-density stainless steel specimens [52]. As a reference, cortical bone typically has a modulus of roughly 12-24 GPa [53,54] depending on sampling orientation, sampling location, age, and other factors. The design parameters used here to fabricate the BCC geometry would negate the stiffness-mismatch between the scaffold and surrounding tissue in a clinical or pre-clinical setting, thereby reducing the likelihood of bone resorption associated with stress-shielding.
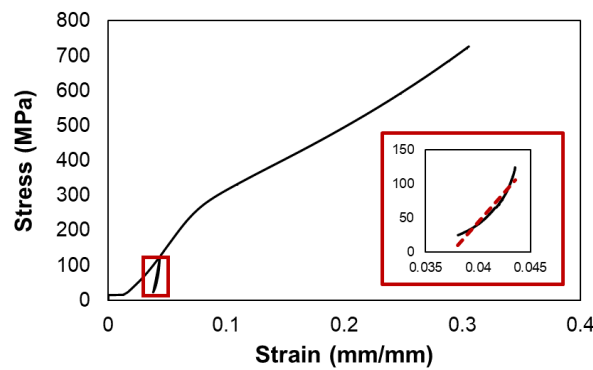

Figure 3: Compliance-corrected mechanical behaviour of the porous stainless steel scaffold via experimental compression. Cylinders were loaded to 50% of their yield point before determining modulus of unloading (E = 17.4 GPa).

3.3 Local strains in mechanical compression trend towards macroscale homogeneity

The elastic modulus from mechanical compression was used to calibrate the finite-element model to assess the magnitude and location of peak strains within the porous scaffold. Under the same loading conditions as the experimental compression, the mean local displacement in the scaffold was measured to be 0.130 mm with similar bulk deformation (Video S2 and Video S3). The distribution of nodal displacements is shown in Figure 4A, where smaller displacements tend to be more common than larger local deformations. In some instances, local displacements at the microscale can be twice that of the average value in the scaffold. This has implications with regards to mechanotransduction [55] and application of fluidic shear [56], potentially leading to preferential cellular activity in a porous material.

The distribution of these displacements through the scaffold is important to understand, as these types of mechanical cues directly influence the production of osteogenic growth factors. Activation of RUNX2 and Osterix, for example, is directly related to local compressive and tensile forces acting on the osteoblast [57]. The introduction of pulsed shear stresses in the osteoblast's local environment is also able to upregulate specific osteogenic factors [57]. The spatial distribution of high-magnitude and low-magnitude displacements within the scaffold interior should therefore mediate the locations of *de novo* bone formation. Figure 4B shows the spatial distribution of nodal displacements on a longitudinal midplane section of the scaffold in compression. Under simulated compressive loading, macroscopic local displacements through the scaffold appear mostly homogenous in nature. The local loading environment for an osteoblast anchored deep within the scaffold compared to an osteoblast anchored to the scaffold periphery should therefore be mostly similar.
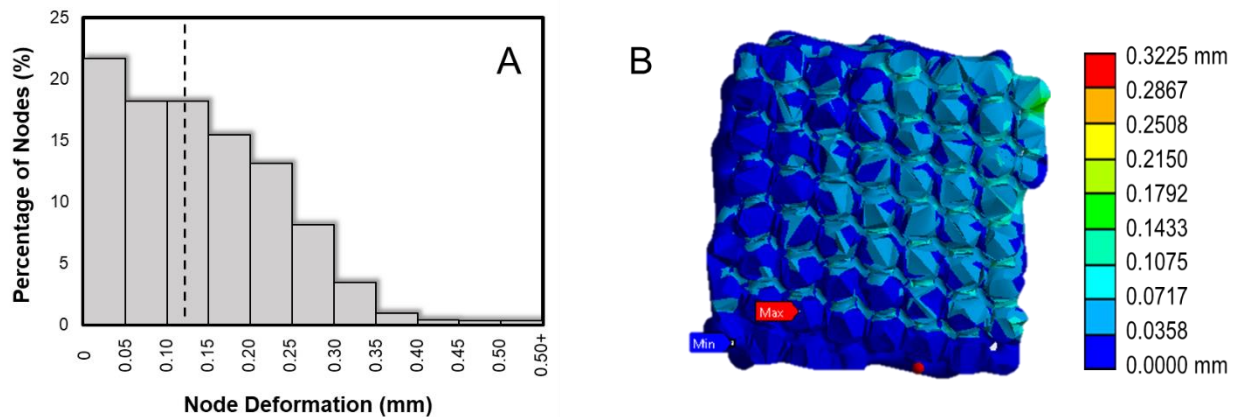

Figure 4: (A) Distribution of nodal displacements in the scaffold during simulated compression up to 12 kN of applied force in ANSYS®. The average nodal displacement (dashed line) at 12 kN of loading is 0.130 mm. Elastic properties of the material were extracted from experimental compression tests of the selective laser melted stainless steel scaffolds. (B) The distribution of local displacements through a longitudinal cross-section of the scaffold. Strain obtained from finite-element model appears mostly homogenous through the midplane of the scaffold under simulated compression. The red and blue arrows represent the regions of highest and lowest displacement, respectively.

In vivo implantation of porous and porous-surfaced materials has previously shown to histomorphometrically outperform plasma-sprayed bone implants [58] and solid implants without surface modification [12]. A correlation between local strain environments within the tissue surrounding porous implants and tissue area fraction has been demonstrated in the 'strain-protected' region [59] that is consistent with the defined osteogenic strain threshold of 1000 $\mu\varepsilon$. Other work has shown that strains and moduli in porous materials are equally dependent on pore size and boundary conditions. For example, nanostructures with larger pore size were shown to have more heterogeneous local strain distributions and higher Weibull moduli [60]. This phenomenon has also been replicated in implants with microporous structures, where simulated compression shows heterogeneous stress distribution across scaffold struts and a discrepancy between mechanical compression and simulated compression [61]. This discrepancy can possibly be attributed to surface roughness, where the stiffness of porous metallic materials can be reduced by smoothing the

surface with an acid-etching process [62,63]. As nodal global values were calibrated based on results from mechanical compression, we are able to somewhat account for the global response of processing defects from selective laser melting, but not able to simulate the effect of defects on local compressive strain.

3.4 Systemic changes can mediate osteogenic strains during resonance excitation

While the viability of therapeutic resonance as a regenerative treatment for bone defects has been recently disputed in the absence of an implant [64,65], it may be important to consider the corresponding vibrational strain of an implant as a driving force for osteogenesis. The investigation of simulated resonance of an implant is required to better understand how systemic variables control the strain distribution throughout the scaffold, and thereby govern local osseointegration.

The model porous implant in this case mimics the response of a threaded dental screw or segmental bone implant, where clamping conditions can anchor the implant in place. Modal analysis was conducted on this implant in the clamped condition following a frequency sweep to map the resonant frequency of the stainless steel implant. In the clamped condition with a 0.5% damping ratio, the natural frequency of the implant was observed to be in the ultrasound range (39.4 kHz). The deformation of the porous implant at this frequency (Figure 5A) was dominated by a nearly pure axial mode shape, with much larger velocities in the axial direction of the cylindrical structure. Peak velocities were observed near the free surface of the implant, while low-velocity resonance is observed within and surrounding the clamped region of the implant. The mean velocity (Figure 5B) was observed to be roughly 39% of the peak value of nodal velocity in the scaffold.
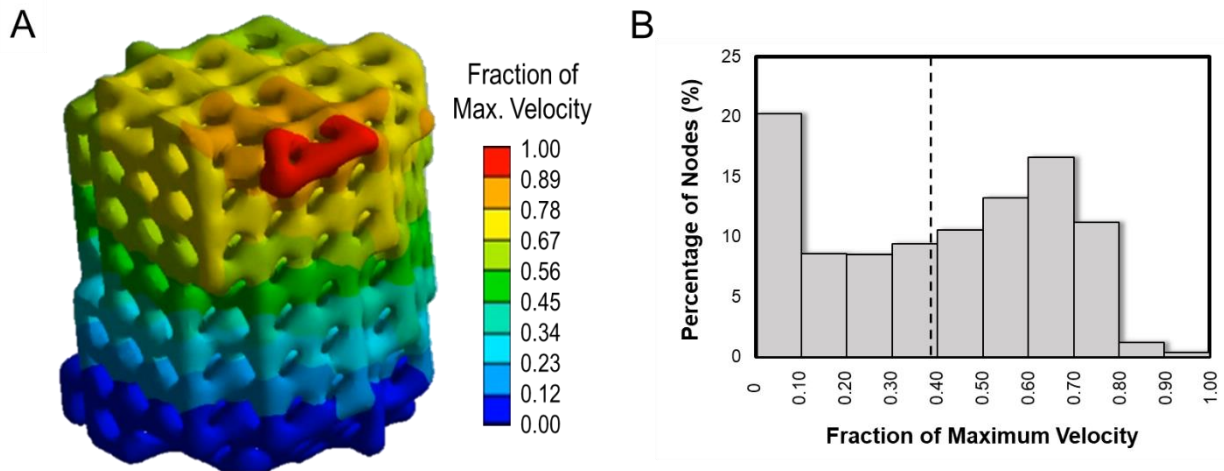

Figure 5: (A) Mode shape in finite-element analysis during resonance of the porous stainless steel scaffold at 39.4 kHz. Modal analysis shows that the shape can be described as an axial mode shape where the velocities are in the axial direction. (B) Distribution of nodal velocities in the scaffold during resonance excitation. The mean velocity during resonance was calculated to be 39% of the peak value in the scaffold. Nodes near the clamped region of the scaffold exhibit low velocity, while nodal velocity increases further away from the clamped region.

3.4.1 Effect of added clamping

The effect of implant clamping was the first systemic variable assessed to evaluate the corresponding strain distribution through the porous implant. To simulate the contact intimacy of a screw in cortical bone, the implant was assessed with and without a fixed support at its base using a damping ratio of 0.5% and an applied vibrational force of 0.5 N. In the absence of the fixed support, the natural frequency was observed to be 51.5 kHz, slightly higher than the natural frequency of the fixed condition (39.4 kHz). By introducing the fixed boundary condition at the base of the scaffold, the mean local strain in the implant increased from 583 με to 1121 με (Figure 6).
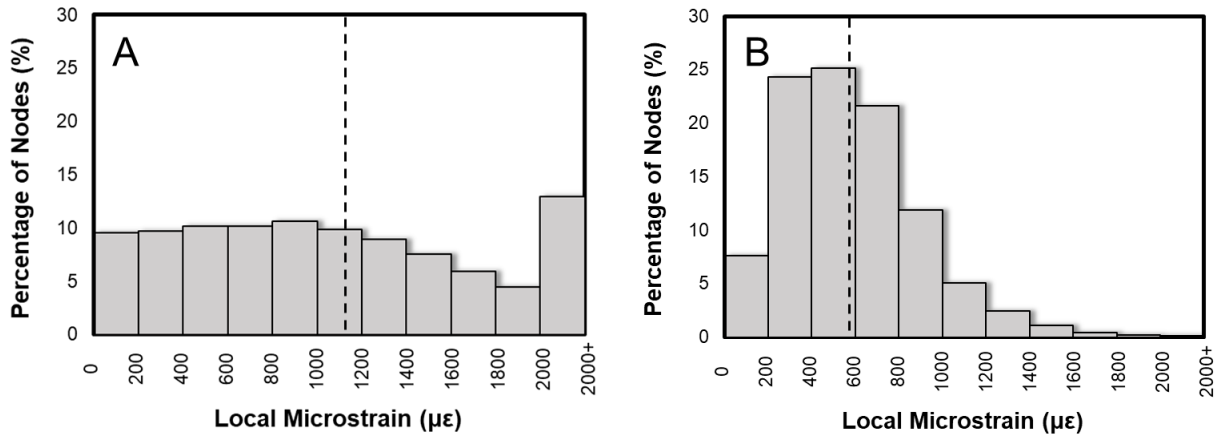

Figure 6: Effect of clamping condition on strain distribution. (A) Nodal strain distribution following clamped resonance excitation at 39.4 kHz, with a vibrational force of 0.5 N and a damping ratio of 0.5%. (B) Nodal strain distribution following unclamped resonance excitation at 51.5 kHz with a vibrational force of 0.5 N and a damping ratio of 0.5%. The addition of clamping at the scaffold base resulted in an upward shift in mean local strain to 1121 με in the scaffold. The scaffold excited in the unclamped condition exhibited a lower standard deviation in local strain compared to the clamped scaffold.

The primary stability between existing cortical bone and a dental implant can be governed by several factors [66]. Depending on the surgical protocol [67] and mandibular bone quality [68], the mechanical interface between a dental implant and pre-existing cortical bone is susceptible to some inherent variability. With the use of a porous implant structure, a notable increase in secondary stability is expected. However, the applicability of resonance excitation at the primary bone-implant interface shows a dependence on primary stability. Since the osteogenic strain threshold of 1000 με is exceeded for a smaller fraction of nodes in the free boundary condition, it must therefore be important to consider the intimacy of contact between the implant and pre-existing cortical bone.

3.4.2 Effect of system damping ratio

While the damping ratio of 0.5% is typically an appropriate estimate for oscillatory decay in the resonance of stainless steel structures [69], attenuation may occur as a result of signal transduction through soft tissue or other means [70]. Here, the authors investigate both positive and negative systemic changes to the damping ratio from the recommended value of 0.5% while keeping the vibrational force and input resonant frequency constant. In resonance systems with a lower

damping ratio (0.3%), local microstrains through the porous scaffold tended to increase. Looking at the distribution of nodal microstrain in the underdamped scenario (Figure 7A), a substantial upward shift can be observed to a mean value of 1868 με and a peak local strain over 27,000 με. Where the strain threshold for microdamage exists around 7000 με [71], this upward shift may be problematic. In the overdamped scenario with a damping ratio of 0.7%, the opposite effect is observed, albeit disproportionately. With a systemically high damping ratio, the mean local strain value decreased to 800 με (Figure 7C) from the reference value of 1121 με at 0.5 N and 0.5% damping (Figure 7B).
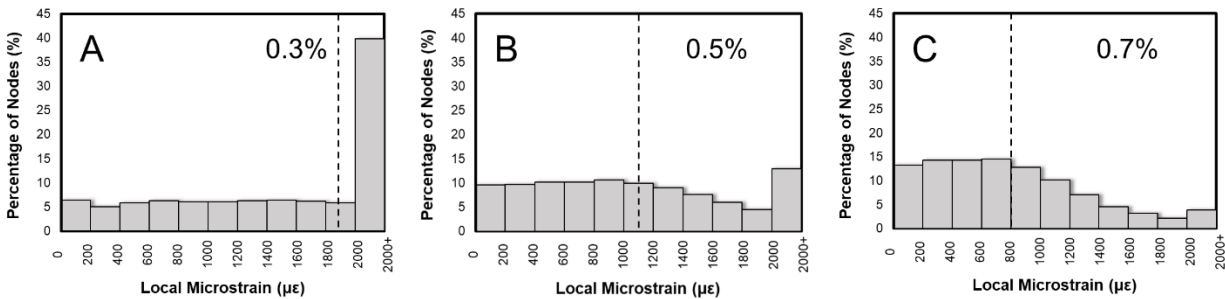

Figure 7: Effect of damping ratio on strain distribution. (A) Nodal strain distribution following resonance excitation at 0.5 N in the clamped condition with a 0.3% damping ratio. (B) Nodal strain distribution following resonance excitation at 0.5 N in the clamped condition with a 0.5% damping ratio. (C) Nodal strain distribution following resonance excitation at 0.5 N in the clamped condition with a 0.7% damping ratio. Increased system damping resulted in an upward shift in average nodal strain, while a proportional decrease in magnitude resulted in lower average local strains in the porous implant.

While system damping is directly interrelated to the natural frequency of the system [72], it is important to note here that a high fraction of nodes remained above the osteogenic threshold at 39.4 kHz after changing the damping ratio. Since a damping ratio of 0.5% is shared for most metals under linear elastic behaviour, the effect of system damping ratio can be expanded to other dental materials such as titanium, where strain values may change with proportionality to the ratio of elastic moduli. Metallic materials are likely to have similarities in their damping ratio, but changes to the systemic damping ratio may be observed for bioceramic implants, for example.

3.4.3 Effect of applied force

The magnitude of the applied vibrational force is likely subject to the efficiency of signal transduction to the implant site. Upon decreasing the applied vibrational force from 0.5 N to 0.3 N, the mean local strain saw a corresponding decrease from 1121 με to 672 με. As expected, the reduced vibratory force produced smaller local displacements in the scaffold. Similarly, an increase in applied force to the scaffold increased the mean local strain to 1569 με. Forces up to 12 N were able to be generated with a transducer directly attached to the stainless steel scaffold. Taking into account thin layers of soft tissue that encapsulate the implant and losses due to signal transduction through the bone, the applied forces used here are within reason.
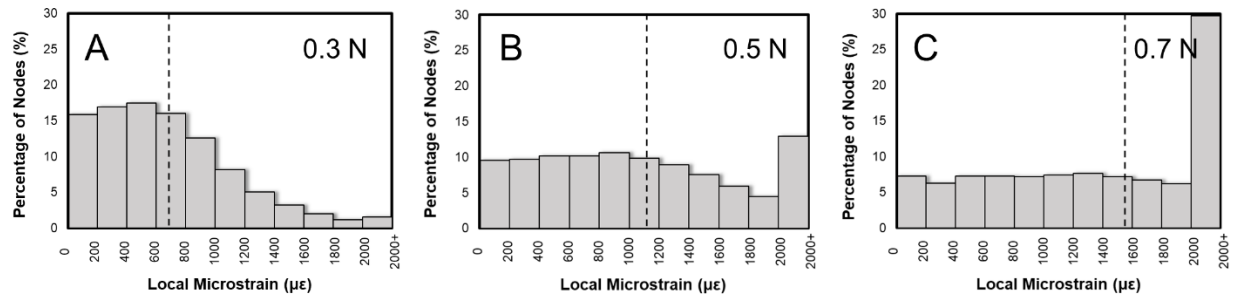
Figure 8: Effect of applied force on strain distribution. (A) Nodal strain distribution following resonance excitation at 0.3 N in the clamped condition with a 0.5% damping ratio. (B) Nodal strain distribution following resonance excitation at 0.5 N in the clamped condition with a 0.5% damping ratio. (C) Nodal strain distribution following resonance excitation at 0.7 N in the clamped condition with a 0.5% damping ratio. Increased vibrational force to 0.7 N resulted in an upward shift in nodal strains from 1121 με to 1569 με. A similar decrease in magnitude resulted in an average local strain of 672 με, below the osteogenic threshold.

Where resonance of experimental bioreactors has produced forces up to 13.5 N by actuation from piezoelectric patches [73], the applied forces of 0.3 N, 0.5 N and 0.7 N used in these experiments should be achievable in implant actuation. Where the applied force from a piezoelectric transducer is proportional to its input voltage at a given excitation frequency, it should also be possible to tune the applied force on the implant to meet interior osteogenic strain thresholds depending on other systemic factors such as system damping, implant material, and implant geometry.

3.4.4 Effect of input frequency

The natural frequency of a given vibrational system is sensitive to changes in the local environment. Under the damping conditions used in these experiments, the frequency spectrum required for resonance remains quite broad (Supplemental S.2). As a result, minor miscalibrations (roughly ± 500 Hz) in the calculation of resonant frequency can be tolerated to maintain osteogenic strains in the scaffold. Larger deviations into the stiffness-controlled (Figure 9A) and mass-controlled (Figure 9C) regions of the frequency-response curve are not so forgiving. When the input frequency was reduced to 31.0 kHz or increased to 42.0 kHz, near-negligible local strains were observed in the scaffold. In both instances, a tenfold reduction in mean local strain was observed by shifting the input frequency out of resonance excitation (Figure 9B). The mean local strain values for the lower frequency and higher frequency were measured to be 34 με and 101 με, respectively.
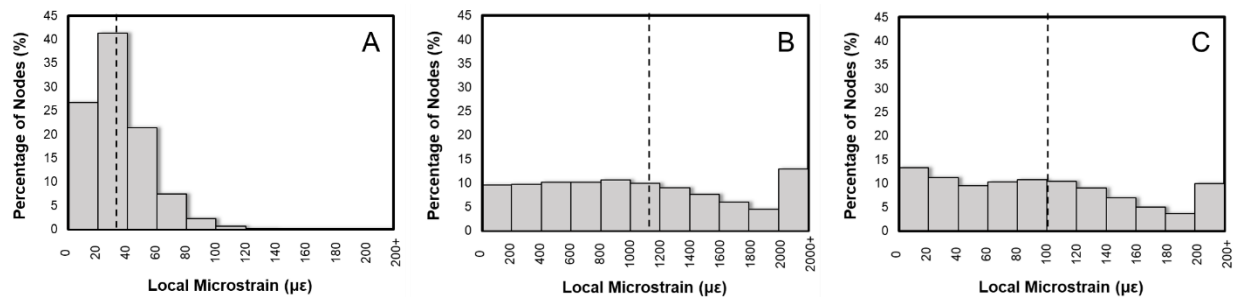
Figure 9: Effect of input frequency on strain distribution. (A) Nodal strain distribution following stiffness-controlled excitation (31.0 kHz) at 0.5 N in the clamped condition with a 0.5% damping ratio. (B) Nodal strain distribution following damping-controlled excitation (39.4 kHz) at 0.5 N in the clamped condition with a 0.5% damping ratio. (C) Nodal strain distribution following mass-controlled excitation (42.0 kHz) at 0.5 N in the clamped condition with a 0.5% damping ratio. In cases above and below the damping-controlled region, the corresponding frequency-response diminishes by a factor of ten in the porous scaffold. In order to have frequency-response in the range of osteogenic strains, it is important to set the input frequency within the damping-controlled region.

3.4.5 Implications

Most applications of therapeutic ultrasound are in the absence of an implant, where the effectiveness of these treatments is widely-debated. In this study, the authors show that the local strain magnitude is incredibly sensitive to the input frequency in the presence of a porous implant. In the stiffness-controlled and mass-controlled regions of the frequency-response curve, local strains in the porous stainless steel scaffold were below the recommended thresholds for both osteogenesis [74] and for woven-to-lamellar transition [75]. Outside of the damping-controlled region, the application of therapeutic resonance likely has little effect on bone regeneration in the vicinity of the implant.

Table 1 summarizes the magnitude of local strains in response to several systemic variables during excitation. Input frequency has the highest degree of sensitivity between all of the tested variables, where a moderate shift away from the natural frequency in either direction resulted in a strain pattern where no node in the structure reached a value of 500 µε. Modulation of the system's damping ratio and input vibrational force had similar sensitivity to one another in the resultant strain. Where the nodal displacement is dependent on the material of the scaffold, it stands to reason that materials with similar elastic moduli, such as tantalum or cobalt-chromium, would undergo similar nodal strains given that they have similar damping ratios [76,77]. By switching to other conventional metal alloys (commercially pure titanium or Ti-6Al-4V, for example), an increase in mean nodal strain on the order of 50-60% would be observed as this is proportional to the ratio of elastic moduli between stainless steel and titanium.

Table 1: Average strains and percentage of strains exceeding 500/1000/1500 µε for each clamped test condition. Systemic changes altering the application of resonance to the implant have the potential to shift local strains above or below osteogenic thresholds during osseointegration.

Frequency (kHz)	Damping Ratio	Applied Force (N)	Average Strain (με)	% of Nodes Above 500 με	% of Nodes Above 1000 με	% of Nodes Above 1500 με
39.4	0.005	0.5	1121	75.6%	49.8%	27.0%
39.4	*0.003*	0.5	1868	85.8%	70.5%	55.1%
39.4	*0.007*	0.5	800	65.5%	30.9%	11.2%
39.4	0.005	*0.3*	672	58.6%	21.2%	6.2%
39.4	0.005	*0.7*	1569	82.9%	64.8%	46.2%
31.0	0.005	0.5	34	0.0%	0.0%	0.0%
42.0	0.005	0.5	101	0.0%	0.0%	0.0%

While the above data references the quantity of nodes reaching the osteogenic threshold, there still lacks spatial definition of where these osteogenic regions are located. An approximation of the longitudinal section plane through the scaffold to visualize strain distributions can be seen in Figure 10A. For the fixed boundary condition shown in Figure 10B with 0.5 N and 0.5% damping ratio, minimal strain is evident in the directly clamped section. Low-strain nodes are also abundant at the point of the implant furthest from the clamped region, where peak strains are present directly above the clamped region. Extending this to clinical application, peak strains under resonance would be most abundant in regions directly adjacent to existing bone-implant contact. Looking at the spatial distribution of normal stresses through the scaffold cross-section, the stress distribution appears homogenous in the X, Y, and Z-components of the normal stress (Figure 10C-E), although the location of minimum and maximum stresses changes depending on which component is analyzed. It is also important to note here that a tenfold increase in normal stress was observed in the Z-component of this normal stress compared to both the X-component and Y-component. This indicates that the strain directionality in the scaffold lies chiefly parallel to the direction of loading in instances of scaffold resonance.
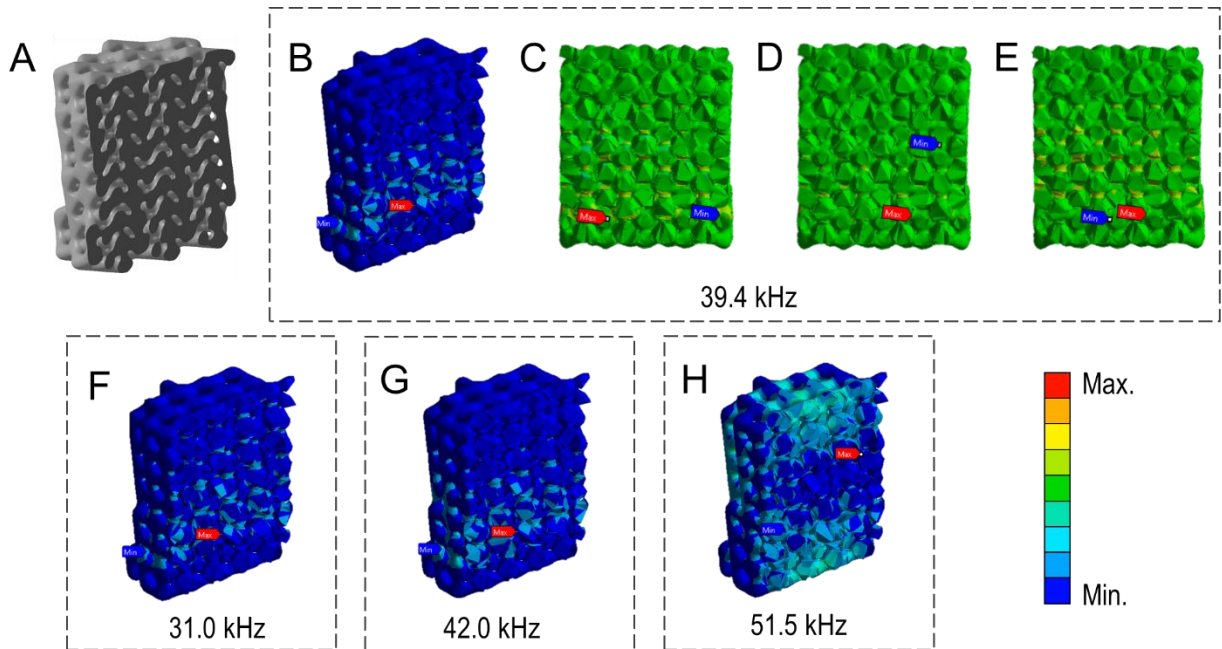
Figure 10: Normalized nodal strain distribution through the porous stainless steel following excitation at 0.5 N and 0.5% damping ratio for varying input frequencies and clamping conditions. (A) Orientation of the longitudinal cross-section. (B) Normalized strain map in the longitudinal section of the scaffold under damping-controlled clamped resonance. Strains appear highest directly above the clamped region. (C) Component of normal stress along the X-axis. (D) Component of normal stress along the Y-axis. (E) Component of normal stress along the Z-axis. While the normalized distributions are very similar, the Z-component of the stress is an order of magnitude higher than the X-component and Y-component. (F) Normalized strain map in the longitudinal section of the scaffold under stiffness-controlled clamped resonance. Despite the variation in strain magnitude, the spatial distribution of strains is similar to that of the damping-controlled case. (G) Normalized strain map in the longitudinal section of the scaffold under mass-controlled clamped resonance. The locations of minimum and maximum strain appear similar to the damping-controlled and stiffness-controlled cases. (H) Normalized strain map in the longitudinal section of the scaffold under unclamped resonance.

The strain distribution is common in all fixed conditions regardless of the input frequency (Figure 10F and 10G), damping ratio, or vibrational force. However, in the case of poor primary stability (Figure 10H), this distribution changes. Here, strains appear symmetric about the midpoint of the scaffold due to the lack of fixed boundary condition at the scaffold base. Peak strains are present at the center of the scaffold's basal planes, while minimum strains are present at the midpoint of the scaffold interior.

When looking at a compound geometry, where additional components are merged with the porous scaffold (like the threaded structure in Figure 11A), there is only a minor influence on the corresponding behaviour in resonance. The mode shape of a scaffold merged with a cylinder at its base (Figure 11B), as an example, is very similar to the mode shape seen when only the scaffold is placed in resonance (Figure 5A). The added mass and stiffness change from this cylinder downshifts the resonant frequency of the compound implant to 37.9 kHz from 39.4 kHz. In any compound implant geometry, such as threaded implants, it is therefore necessary to determine the

resonant frequency of the implant prior to insertion. Looking at a sample cross-section of the scaffold (Figure 11C), the von Mises stress distribution (Figure 11D) does not show any evidence of stress concentration at the interface between the porous construct and cylindrical base under normal clamped conditions. It stands to reason that similar geometric alterations to the implant will only minimally influence the stress distribution.
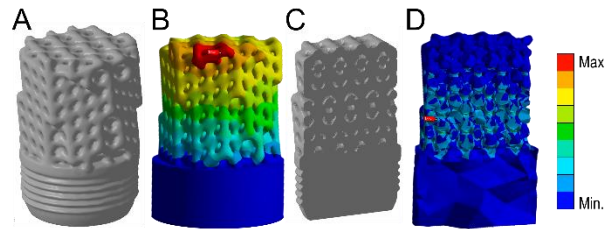

Figure 11: The effect of an abrupt change in scaffold geometry on resonance behaviour. (A) Sample model of a threaded screw-type implant as a model of abrupt geometrical shift. (B) Corresponding mode shape of the compound porous implant structure at 37.9 kHz with the clamping applied to a portion of the cylindrical base. The mode shape is nearly identical to that of the scaffold without the cylindrical base. (C) Cross-sectional plane of the compound implant geometry. (D) Von Mises stress distribution within this cross-section. The addition of a geometrical interface does not result in stress concentration at any point.

In these experiments, the authors assess the simulated elastic response of a model scaffold under resonance. From our observations, we estimate that the investigated sample volume is greater than the representative volume element. If in future applications, scaffold size should be lowered, e.g. for a porous layer on solid implant surfaces, size will affect the structure's material response. Increasing elongation rather than beam bending, and modified boundary conditions will both determine intensity of this effect [78–80]. Further investigation should look at the identification of representative volume elements with varying meshing strategies to assess both the local and global response of these porous materials in resonance.

For bone regeneration surrounding an implant, the application of therapeutic resonance shows promise in terms of controlled cyclical application of osteogenic strains throughout a porous material. This may have relevance in bone regeneration of mandibular dental implants or for repair of segmental bone defects where minimal soft tissue is present around bony protrusions. With the application of a piezoelectric transducer and sufficient bone transduction, it may be possible to cause controlled resonance of a porous metallic implant to induce strains within the range of favourable osteogenesis, cellular response, and maturation.

4 Conclusions

The application of therapeutic ultrasound to promote osteogenesis shows potential in cases where an implant is present at the defect site. We demonstrate in this work that the application of therapeutic ultrasound in damping-controlled implant resonance is able to meet local strain thresholds for osteogenesis according to the mechanostat theory. The magnitude of strains experienced under implant vibration are highly sensitive to the input frequency, with some sensitivity originating from system damping and applied vibrational force. Examination of the fixed boundary condition for a screw-type implant shows that primary stability, as modeled by clamping of the scaffold base, is a governing factor for the natural frequency of the system. In

implants with high primary stability, peak strains were observed directly adjacent to points of bone-implant contact. This phenomenon was independent of system damping ratio, applied force, or input frequency. In the absence of primary stability, peak strains were observed at the midpoint of the top and bottom faces of the implant with symmetry about the scaffold midplanes. The authors suggest that the application of therapeutic implant resonance can have favourable effects on osteogenesis by subjecting the bone to the required mechanical stimulus for both bone formation and maturation.

Future work can aim to extend these principles in a pre-clinical setting or with refined representative volume elements in simulation. It will also be worthwhile to investigate deformation in femoral or tibial implants through loads experienced in the gait cycle with greater detail, as mechanical deformation of the implant happens naturally with each step of the patient at 1 Hz [74] and is beneficial for stimulation of bone growth. Early mobilization of a patient has multiple positive effects, especially when these factors are supplemented with therapeutic concepts. For both therapeutic resonance and mechanical gait, implants in various locations along the lower extremity should target the 1000 $\mu\varepsilon$ threshold by adapting implant stiffness and topology.

5 Acknowledgements

6 References

(1) Huiskes, R.; Weinans, H.; Rietbergen, B. van. The Relationship Between Stress Shielding and Bone Resorption Around Total Hip Stems and the Effects of Flexible Materials. *Clin Orthop Relat R* **1992**, *274* (NA;), 124–134. https://doi.org/10.1097/00003086-199201000-00014.

(2) Bauer, T. W.; Schils, J. The Pathology of Total Joint Arthroplasty. *Skeletal Radiol* **1999**, *28* (9), 483–497. https://doi.org/10.1007/s002560050552.

(3) Nagels, J.; Stokdijk, M.; Rozing, P. M. Stress Shielding and Bone Resorption in Shoulder Arthroplasty. *J Shoulder Elb Surg* **2003**, *12* (1), 35–39. https://doi.org/10.1067/mse.2003.22.

(4) Arabnejad, S.; Johnston, B.; Tanzer, M.; Pasini, D. Fully Porous 3D Printed Titanium Femoral Stem to Reduce Stress-shielding Following Total Hip Arthroplasty. *J Orthopaed Res* **2017**, *35* (8), 1774–1783. https://doi.org/10.1002/jor.23445.

(5) Bandyopadhyay, A.; Espana, F.; Balla, V. K.; Bose, S.; Ohgami, Y.; Davies, N. M. Influence of Porosity on Mechanical Properties and in Vivo Response of Ti6Al4V Implants. *Acta Biomater* **2010**, *6* (4), 1640–1648. https://doi.org/10.1016/j.actbio.2009.11.011.

(6) Wang, X.; Xu, S.; Zhou, S.; Xu, W.; Leary, M.; Choong, P.; Qian, M.; Brandt, M.; Xie, Y. M. Topological Design and Additive Manufacturing of Porous Metals for Bone Scaffolds and Orthopaedic Implants: A Review. *Biomaterials* **2016**, *83*, 127–141. https://doi.org/10.1016/j.biomaterials.2016.01.012.

(7) Hashin, Z. Analysis of Composite Materials—A Survey. *J Appl Mech* **1983**, *50* (3), 481–505. https://doi.org/10.1115/1.3167081.

(8) Deering, J.; Clifford, A.; D'Elia, A.; Zhitomirsky, I.; Grandfield, K. Composite Dip Coating Improves Biocompatibility of Porous Metallic Scaffolds. *Mater Lett* **2020**, *274*, 128057. https://doi.org/10.1016/j.matlet.2020.128057.

(9) Clifford, A.; D'Elia, A.; Deering, J.; Lee, B. E. J.; Grandfield, K.; Zhitomirsky, I. Electrochemical Fabrication and Characterization of Pectin Hydrogel Composite Materials for Bone Tissue Repair. *Acs Appl Polym Mater* **2020**, *2* (8), 3390–3396. https://doi.org/10.1021/acsapm.0c00480.

(10) D'Elia, A.; Deering, J.; Clifford, A.; Lee, B. E. J.; Grandfield, K.; Zhitomirsky, I. Electrophoretic Deposition of Polymethylmethacrylate and Composites for Biomedical Applications. *Colloids Surfaces B Biointerfaces* **2019**, *188*, 110763. https://doi.org/10.1016/j.colsurfb.2019.110763.

(11) Kilian, O.; Schnettler, R. Endoprothetik. *undefined* **2009**, 63–88. https://doi.org/10.1515/9783110211993.63.

(12) Wang, H.; Su, K.; Su, L.; Liang, P.; Ji, P.; Wang, C. The Effect of 3D-Printed Ti6Al4V Scaffolds with Various Macropore Structures on Osteointegration and Osteogenesis: A Biomechanical Evaluation. *J Mech Behav Biomed* **2018**, *88* (J. Mech. Behav. Biomed. Mater. 34 2014), 488–496. https://doi.org/10.1016/j.jmbbm.2018.08.049.

(13) Pearce, A.; Richards, R.; Milz, S.; Schneider, E.; Pearce, S. Animal Models for Implant Biomaterial Research in Bone: A Review. *European Cells Mater* **2007**, *13*, 1–10. https://doi.org/10.22203/ecm.v013a01.

(14) Heinl, P.; Müller, L.; Körner, C.; Singer, R. F.; Müller, F. A. Cellular Ti–6Al–4V Structures with Interconnected Macro Porosity for Bone Implants Fabricated by Selective Electron Beam Melting. *Acta Biomater* **2008**, *4* (5), 1536–1544. https://doi.org/10.1016/j.actbio.2008.03.013.

(15) Pham, A.; Kelly, C.; Gall, K. Free Boundary Effects and Representative Volume Elements in 3D Printed Ti–6Al–4V Gyroid Structures. *J Mater Res* **2020**, *35* (19), 2547–2555. https://doi.org/10.1557/jmr.2020.105.

(16) Liu, F.; Mao, Z.; Zhang, P.; Zhang, D. Z.; Jiang, J.; Ma, Z. Functionally Graded Porous Scaffolds in Multiple Patterns: New Design Method, Physical and Mechanical Properties. *Mater Design* **2018**, *160* (Biomaterials 23 2002), 849–860. https://doi.org/10.1016/j.matdes.2018.09.053.

(17) Chang, J. Z.-C.; Tsai, P.-I.; Kuo, M. Y.-P.; Sun, J.-S.; Chen, S.-Y.; Shen, H.-H. Augmentation of DMLS Biomimetic Dental Implants with Weight-Bearing Strut to Balance of Biologic and Mechanical Demands: From Bench to Animal. *Materials* **2019**, *12* (1), 164. https://doi.org/10.3390/ma12010164.

(18) Wang, X.; Lin, Q.; Zhang, T.; Wang, X.; Cheng, K.; Gao, M.; Xia, P.; Li, X. Low-Intensity Pulsed Ultrasound Promotes Chondrogenesis of Mesenchymal Stem Cells via Regulation of Autophagy. *Stem Cell Res Ther* **2019**, *10* (1), 41. https://doi.org/10.1186/s13287-019-1142-z.

(19) Lv, Y.; Zhao, P.; Chen, G.; Sha, Y.; Yang, L. Effects of Low-Intensity Pulsed Ultrasound on Cell Viability, Proliferation and Neural Differentiation of Induced Pluripotent Stem Cells-Derived Neural Crest Stem Cells. *Biotechnol Lett* **2013**, *35* (12), 2201–2212. https://doi.org/10.1007/s10529-013-1313-4.

(20) Lv, Y.; Nan, P.; Chen, G.; Sha, Y.; Xia, B.; Yang, L. In Vivo Repair of Rat Transected Sciatic Nerve by Low-Intensity Pulsed Ultrasound and Induced Pluripotent Stem Cells-Derived Neural Crest Stem Cells. *Biotechnol Lett* **2015**, *37* (12), 2497–2506. https://doi.org/10.1007/s10529-015-1939-5.

(21) Mittelstein, D. R.; Ye, J.; Schibber, E. F.; Roychoudhury, A.; Martinez, L. T.; Fekrazad, M. H.; Ortiz, M.; Lee, P. P.; Shapiro, M. G.; Gharib, M. Selective Ablation of Cancer Cells with Low Intensity Pulsed Ultrasound. *Appl Phys Lett* **2020**, *116* (1), 013701. https://doi.org/10.1063/1.5128627.

(22) Tempany, C. M. C.; McDannold, N. J.; Hynynen, K.; Jolesz, F. A. Focused Ultrasound Surgery in Oncology: Overview and Principles. *Radiology* **2011**, *259* (1), 39–56. https://doi.org/10.1148/radiol.11100155.

(23) Kennedy, J. E. High-Intensity Focused Ultrasound in the Treatment of Solid Tumours. *Nat Rev Cancer* **2005**, *5* (4), 321–327. https://doi.org/10.1038/nrc1591.

(24) LuTheryn, G.; Glynne-Jones, P.; Webb, J. S.; Carugo, D. Ultrasound-mediated Therapies for the Treatment of Biofilms in Chronic Wounds: A Review of Present Knowledge. *Microb Biotechnol* **2020**, *13* (3), 613–628. https://doi.org/10.1111/1751-7915.13471.

(25) Yu, H.; Liu, Y.; Li, L.; Guo, Y.; Xie, Y.; Cheng, Y.; Yao, W. Ultrasound-Involved Emerging Strategies for Controlling Foodborne Microbial Biofilms. *Trends Food Sci Tech* **2019**, *96*, 91–101. https://doi.org/10.1016/j.tifs.2019.12.010.

(26) Romano, C. L.; Romano, D.; Logoluso, N. Low-Intensity Pulsed Ultrasound for the Treatment of Bone Delayed Union or Nonunion: A Review. *Ultrasound Medicine Biology* **2009**, *35* (4), 529–536. https://doi.org/10.1016/j.ultrasmedbio.2008.09.029.

(27) Nolte, P. A.; Krans, A. van der; Patka, P.; Janssen, I. M. C.; Ryaby, J. P.; Albers, G. H. R. Low-Intensity Pulsed Ultrasound in the Treatment of Nonunions. *J Trauma Inj Infect Critical Care* **2001**, *51* (4), 693–703. https://doi.org/10.1097/00005373-200110000-00012.

(28) Heckman, J. D.; Ryaby, J. P.; McCabe, J.; Frey, J. J.; Kilcoyne, R. F. Acceleration of Tibial Fracture-Healing by Non-Invasive, Low-Intensity Pulsed Ultrasound. *J Bone Jt Surg* **1994**, *76* (1), 26–34. https://doi.org/10.2106/00004623-199401000-00004.

(29) Kristiansen, T. K.; RYABY, J. P.; McCABE, J.; FREY, J. J.; Roe, L. R. Accelerated Healing of Distal Radial Fractures with the Use of Specific, Low-Intensity Ultrasound. A Multicenter, Prospective, Randomized, Double-Blind, Placebo-Controlled Study*. *J Bone Jt Surg* **1997**, *79* (7), 961–973. https://doi.org/10.2106/00004623-199707000-00002.

(30) Harrison, A.; Lin, S.; Pounder, N.; Mikuni-Takagaki, Y. Mode & Mechanism of Low Intensity Pulsed Ultrasound (LIPUS) in Fracture Repair. *Ultrasonics* **2016**, *70*, 45–52. https://doi.org/10.1016/j.ultras.2016.03.016.

(31) Lu, H.; Qin, L.; Cheung, W.; Lee, K.; Wong, W.; Leung, K. Low-Intensity Pulsed Ultrasound Accelerated Bone-Tendon Junction Healing Through Regulation of Vascular Endothelial Growth Factor Expression and Cartilage Formation. *Ultrasound Medicine Biology* **2008**, *34* (8), 1248–1260. https://doi.org/10.1016/j.ultrasmedbio.2008.01.009.

(32) Deering, J.; Presas, A.; Lee, B. E. J.; Valentin, D.; Yu, B.; Heiss, C.; Grandfield, K.; Bosbach, W. A. Response of Saos-2 Osteoblast-like Cells to Kilohertz-Resonance Excitation in Porous Metallic Scaffolds. *J Mech Behav Biomed* **2020**, *106*, 103726. https://doi.org/10.1016/j.jmbbm.2020.103726.

(33) Gebauer, D.; Mayr, E.; Orthner, E.; Ryaby, J. P. Low-Intensity Pulsed Ultrasound: Effects on Nonunions. *Ultrasound Medicine Biology* **2005**, *31* (10), 1391–1402. https://doi.org/10.1016/j.ultrasmedbio.2005.06.002.

(34) Pounder, N. M.; Harrison, A. J. Low Intensity Pulsed Ultrasound for Fracture Healing: A Review of the Clinical Evidence and the Associated Biological Mechanism of Action. *Ultrasonics* **2008**, *48* (4), 330–338. https://doi.org/10.1016/j.ultras.2008.02.005.

(35) Takayama, T.; Suzuki, N.; Ikeda, K.; Shimada, T.; Suzuki, A.; Maeno, M.; Otsuka, K.; Ito, K. Low-Intensity Pulsed Ultrasound Stimulates Osteogenic Differentiation in ROS 17/2.8 Cells. *Life Sci* **2007**, *80* (10), 965–971. https://doi.org/10.1016/j.lfs.2006.11.037.

(36) Maung, W. M.; Nakata, H.; Miura, M.; Miyasaka, M.; Kim, Y.-K.; Kasugai, S.; Kuroda, S. Low-Intensity Pulsed Ultrasound Stimulates Osteogenic Differentiation of Periosteal Cells In Vitro. *Tissue Eng Pt A* **2020**. https://doi.org/10.1089/ten.tea.2019.0331.

(37) Warden, S. J.; Favaloro, J. M.; Bennell, K. L.; McMeeken, J. M.; Ng, K.-W.; Zajac, J. D.; Wark, J. D. Low-Intensity Pulsed Ultrasound Stimulates a Bone-Forming Response in UMR-106 Cells. *Biochem Bioph Res Co* **2001**, *286* (3), 443–450. https://doi.org/10.1006/bbrc.2001.5412.

(38) Naruse, K.; Miyauchi, A.; Itoman, M.; Mikuni-Takagaki, Y. Distinct Anabolic Response of Osteoblast to Low-Intensity Pulsed Ultrasound. *J Bone Miner Res* **2003**, *18* (2), 360–369. https://doi.org/10.1359/jbmr.2003.18.2.360.

(39) Kobayashi, Y.; Sakai, D.; Iwashina, T.; Iwabuchi, S.; Mochida, J. Low-Intensity Pulsed Ultrasound Stimulates Cell Proliferation, Proteoglycan Synthesis and Expression of Growth Factor-Related Genes in Human Nucleus Pulposus Cell Line. *European Cells Mater* **2009**, *17*, 11–22. https://doi.org/10.22203/ecm.v017a02.

(40) Xue, H.; Zheng, J.; Cui, Z.; Bai, X.; Li, G.; Zhang, C.; He, S.; Li, W.; Lajud, S. A.; Duan, Y.; Zhou, H. Low-Intensity Pulsed Ultrasound Accelerates Tooth Movement via Activation of the BMP-2 Signaling Pathway. *Plos One* **2013**, *8* (7), e68926. https://doi.org/10.1371/journal.pone.0068926.

(41) Lanyon, L. E. Functional Strain as a Determinant for Bone Remodeling. *Calcified Tissue Int* **1984**, *36* (Suppl 1), S56–S61. https://doi.org/10.1007/bf02406134.

(42) Burr, D. B.; Martin, R. B.; Schaffler, M. B.; Radin, E. L. Bone Remodeling in Response to in Vivo Fatigue Microdamage. *J Biomech* **1985**, *18* (3), 189–200. https://doi.org/10.1016/0021-9290(85)90204-0.

(43) Kotha, S. P.; Hsieh, Y.-F.; Strigel, R. M.; Müller, R.; Silva, M. J. Experimental and Finite Element Analysis of the Rat Ulnar Loading Model—Correlations between Strain and Bone Formation Following Fatigue Loading. *J Biomech* **2004**, *37* (4), 541–548. https://doi.org/10.1016/j.jbiomech.2003.08.009.

(44) Rubin, C. T.; Lanyon, L. E. Osteoregulatory Nature of Mechanical Stimuli: Function as a Determinant for Adaptive Remodeling in Bone. *J Orthopaed Res* **1987**, *5* (2), 300–310. https://doi.org/10.1002/jor.1100050217.

(45) Frost, H. M. Bone "Mass" and the "Mechanostat": A Proposal. *Anatomical Rec* **1987**, *219* (1), 1–9. https://doi.org/10.1002/ar.1092190104.

(46) Forwood, M. R.; Turner, C. H. Skeletal Adaptations to Mechanical Usage: Results from Tibial Loading Studies in Rats. *Bone* **1995**, *17* (4), S197–S205. https://doi.org/10.1016/8756-3282(95)00292-l.

(47) Presas, A.; Valentin, D.; Egusquiza, E.; Valero, C.; Egusquiza, M.; Bossio, M. Accurate Determination of the Frequency Response Function of Submerged and Confined Structures by Using PZT-Patches†. *Sensors* **2017**, *17* (3), 660. https://doi.org/10.3390/s17030660.

(48) Melancon, D.; Bagheri, Z. S.; Johnston, R. B.; Liu, L.; Tanzer, M.; Pasini, D. Mechanical Characterization of Structurally Porous Biomaterials Built via Additive Manufacturing: Experiments, Predictive Models, and Design Maps for Load-Bearing Bone Replacement Implants. *Acta Biomater* **2017**, *63*, 350–368. https://doi.org/10.1016/j.actbio.2017.09.013.

(49) Warnke, P. H.; Douglas, T.; Wollny, P.; Sherry, E.; Steiner, M.; Galonska, S.; Becker, S. T.; Springer, I. N.; Wiltfang, J.; Sivananthan, S. Rapid Prototyping: Porous Titanium Alloy Scaffolds Produced by Selective Laser Melting for Bone Tissue Engineering. *Tissue Eng Part C Methods* **2009**, *15* (2), 115–124. https://doi.org/10.1089/ten.tec.2008.0288.

(50) Ashby, M. F.; Medalist, R. F. M. The Mechanical Properties of Cellular Solids. *Metallurgical Transactions* **1983**, *14* (9), 1755–1769. https://doi.org/10.1007/bf02645546.

(51) Deshpande, V. S.; Ashby, M. F.; Fleck, N. A. Foam Topology: Bending versus Stretching Dominated Architectures. *Acta Mater* **2001**, *49* (6), 1035–1040. https://doi.org/10.1016/s1359-6454(00)00379-7.

(52) Disegi, J. A.; Eschbach, L. Stainless Steel in Bone Surgery. *Inj* **2000**, *31*, D2–D6. https://doi.org/10.1016/s0020-1383(00)80015-7.

(53) Turner, C. H.; Rho, J.; Takano, Y.; Tsui, T. Y.; Pharr, G. M. The Elastic Properties of Trabecular and Cortical Bone Tissues Are Similar: Results from Two Microscopic Measurement Techniques. *J Biomech* **1999**, *32* (4), 437–441. https://doi.org/10.1016/s0021-9290(98)00177-8.

(54) Ashman, R. B.; Cowin, S. C.; Buskirk, W. C. V.; Rice, J. C. A Continuous Wave Technique for the Measurement of the Elastic Properties of Cortical Bone. *J Biomech* **1984**, *17* (5), 349–361. https://doi.org/10.1016/0021-9290(84)90029-0.

(55) Duncan, R. L.; Turner, C. H. Mechanotransduction and the Functional Response of Bone to Mechanical Strain. *Calcified Tissue Int* **1995**, *57* (5), 344–358. https://doi.org/10.1007/bf00302070.

(56) Owan, I.; Burr, D. B.; Turner, C. H.; Qiu, J.; Tu, Y.; Onyia, J. E.; Duncan, R. L. Mechanotransduction in Bone: Osteoblasts Are More Responsive to Fluid Forces than Mechanical Strain. *Am J Physiol-cell Ph* **1997**, *273* (3), C810–C815. https://doi.org/10.1152/ajpcell.1997.273.3.c810.

(57) Rutkovskiy, A.; Stensløkken, K.-O.; Vaage, I. J. Osteoblast Differentiation at a Glance. *Medical Sci Monit Basic Res* **2016**, *22*, 95–106. https://doi.org/10.12659/msmbr.901142.

(58) Simmons, C. A.; Valiquette, N.; Pilliar, R. M. Osseointegration of Sintered Porous-surfaced and Plasma Spray–Coated Implants: An Animal Model Study of Early Postimplantation Healing Response and Mechanical Stability. *J Biomed Mater Res* **1999**, *47* (2), 127–138. https://doi.org/10.1002/(sici)1097-4636(199911)47:2<127::aid-jbm3>3.0.co;2-c.

(59) Simmons, C. A.; Meguid, S. A.; Pilliar, R. M. Differences in Osseointegration Rate Due to Implant Surface Geometry Can Be Explained by Local Tissue Strains. *J Orthopaed Res* **2001**, *19* (2), 187–194. https://doi.org/10.1016/s0736-0266(00)90006-8.

(60) Deng, S.; Wang, Y.; Zhuang, G.; Zhong, X.; Wei, Z.; Yao, Z.; Wang, J. Micromechanical Simulation of the Pore Size Effect on the Structural Stability of Brittle Porous Materials with Bicontinuous Morphology. *Phys Chem Chem Phys* **2019**, *21* (24), 12895–12904. https://doi.org/10.1039/c9cp01582e.

(61) Zhang, B.; Pei, X.; Zhou, C.; Fan, Y.; Jiang, Q.; Ronca, A.; D'Amora, U.; Chen, Y.; Li, H.; Sun, Y.; Zhang, X. The Biomimetic Design and 3D Printing of Customized Mechanical

Properties Porous Ti6Al4V Scaffold for Load-Bearing Bone Reconstruction. *Mater Design* **2018**, *152*, 30–39. https://doi.org/10.1016/j.matdes.2018.04.065.

(62) Pyka, G.; Burakowski, A.; Kerckhofs, G.; Moesen, M.; Bael, S. V.; Schrooten, J.; Wevers, M. Surface Modification of Ti6Al4V Open Porous Structures Produced by Additive Manufacturing. *Adv Eng Mater* **2012**, *14* (6), 363–370. https://doi.org/10.1002/adem.201100344.

(63) Pyka, G.; Kerckhofs, G.; Papantoniou, I.; Speirs, M.; Schrooten, J.; Wevers, M. Surface Roughness and Morphology Customization of Additive Manufactured Open Porous Ti6Al4V Structures. *Materials* **2013**, *6* (10), 4737–4757. https://doi.org/10.3390/ma6104737.

(64) Busse, J. W.; Bhandari, M.; Einhorn, T. A.; Schemitsch, E.; Heckman, J. D.; Tornetta, P.; Leung, K.-S.; Heels-Ansdell, D.; Makosso-Kallyth, S.; Rocca, G. J. D.; Jones, C. B.; Guyatt, G. H. Re-Evaluation of Low Intensity Pulsed Ultrasound in Treatment of Tibial Fractures (TRUST): Randomized Clinical Trial. *Bmj* **2016**, *355*, i5351. https://doi.org/10.1136/bmj.i5351.

(65) Poolman, R. W.; Agoritsas, T.; Siemieniuk, R. A. C.; Harris, I. A.; Schipper, I. B.; Mollon, B.; Smith, M.; Albin, A.; Nador, S.; Sasges, W.; Schandelmaier, S.; Lytvyn, L.; Kuijpers, T.; Beers, L. W. A. H. van; Verhofstad, M. H. J.; Vandvik, P. O. Low Intensity Pulsed Ultrasound (LIPUS) for Bone Healing: A Clinical Practice Guideline. *Bmj* **2017**, *356*, j576. https://doi.org/10.1136/bmj.j576.

(66) Tanaka, K.; Sailer, I.; Iwama, R.; Yamauchi, K.; Nogami, S.; Yoda, N.; Takahashi, T. Relationship between Cortical Bone Thickness and Implant Stability at the Time of Surgery and Secondary Stability after Osseointegration Measured Using Resonance Frequency Analysis. *J Periodontal Implant Sci* **2018**, *48* (6), 360–372. https://doi.org/10.5051/jpis.2018.48.6.360.

(67) Turkyilmaz, I.; Aksoy, U.; McGlumphy, E. A. Two Alternative Surgical Techniques for Enhancing Primary Implant Stability in the Posterior Maxilla: A Clinical Study Including Bone Density, Insertion Torque, and Resonance Frequency Analysis Data. *Clin Implant Dent R* **2008**, *10* (4), 231–237. https://doi.org/10.1111/j.1708-8208.2008.00084.x.

(68) Oh, J.-S.; Kim, S.-G. Clinical Study of the Relationship between Implant Stability Measurements Using Periotest and Osstell Mentor and Bone Quality Assessment. *Oral Surg Oral Medicine Oral Pathology Oral Radiology* **2012**, *113* (3), e35–e40. https://doi.org/10.1016/j.tripleo.2011.07.003.

(69) Valentín, D.; Presas, A.; Egusquiza, E.; Valero, C. Experimental Study on the Added Mass and Damping of a Disk Submerged in a Partially Fluid-Filled Tank with Small Radial Confinement. *J Fluid Struct* **2014**, *50*, 1–17. https://doi.org/10.1016/j.jfluidstructs.2014.06.006.

(70) Xu, K.; Liu, D.; Ta, D.; Hu, B.; Wang, W. Quantification of Guided Mode Propagation in Fractured Long Bones. *Ultrasonics* **2014**, *54* (5), 1210–1218. https://doi.org/10.1016/j.ultras.2013.09.015.

(71) Robling, A. G.; Castillo, A. B.; Turner, C. H. Biomechanical and Molecular Regulation of Bone Remodeling. *Annu Rev Biomed Eng* **2006**, *8* (1), 455–498. https://doi.org/10.1146/annurev.bioeng.8.061505.095721.

(72) Lee, I.-W.; Kim, D.-O.; Jung, G.-H. Natural Frequency and Mode Shape Sensitivities OF Damped Systems: Part I, Distincy Natural Frequencies. *J Sound Vib* **1999**, *223* (3), 399–412. https://doi.org/10.1006/jsvi.1998.2129.

(73) Valentin, D.; Presas, A.; Roehr, C.; Mele, E.; Biehl, C.; Heiss, C.; Bosbach, W. A. On the Quantification of Local Power Densities in a New Vibration Bioreactor. *Plos One* **2021**, *16* (1), e0245768. https://doi.org/10.1371/journal.pone.0245768.

(74) Rubin, C. T.; Lanyon, L. E. Regulation of Bone Mass by Mechanical Strain Magnitude. *Calcified Tissue Int* **1985**, *37* (4), 411–417. https://doi.org/10.1007/bf02553711.

(75) Sugiyama, T.; Meakin, L. B.; Browne, W. J.; Galea, G. L.; Price, J. S.; Lanyon, L. E. Bones' Adaptive Response to Mechanical Loading Is Essentially Linear between the Low Strains Associated with Disuse and the High Strains Associated with the Lamellar/Woven Bone Transition. *J Bone Miner Res* **2012**, *27* (8), 1784–1793. https://doi.org/10.1002/jbmr.1599.

(76) Zhang, J.; Perez, R. J.; Lavernia, E. J. Documentation of Damping Capacity of Metallic, Ceramic and Metal-Matrix Composite Materials. *J Mater Sci* **1993**, *28* (9), 2395–2404. https://doi.org/10.1007/bf01151671.

(77) Blevins, R. D. *Flow-Induced Vibration*; Van Nostrand Reinhold: New York, 1990.

(78) Kanit, T.; Forest, S.; Galliet, I.; Mounoury, V.; Jeulin, D. Determination of the Size of the Representative Volume Element for Random Composites: Statistical and Numerical Approach. *Int J Solids Struct* **2003**, *40* (13–14), 3647–3679. https://doi.org/10.1016/s0020-7683(03)00143-4.

(79) Dirrenberger, J.; Forest, S.; Jeulin, D. Towards Gigantic RVE Sizes for 3D Stochastic Fibrous Networks. *Int J Solids Struct* **2014**, *51* (2), 359–376. https://doi.org/10.1016/j.ijsolstr.2013.10.011.

(80) Bosbach, W. A. The Elastic Behaviour of Sintered Metallic Fibre Networks: A Finite Element Study by Beam Theory. *Plos One* **2015**, *10* (11), e0143011. https://doi.org/10.1371/journal.pone.0143011.

Implant Resonance and the Mechanostat Theory: Applications of Therapeutic Ultrasound for Porous Metallic Scaffolds

Joseph Deering[1*], Alexandre Presas[2], Bosco Yu[1], David Valentin[2], Christian Heiss[3,4], Wolfram A. Bosbach[3,4], Kathryn Grandfield[1,5*]

[1] Department of Materials Science and Engineering, McMaster University, Hamilton, ON, Canada
[2] Center for Industrial Diagnostics and Fluid Dynamics (CDIF), Polytechnic University of Catalonia (UPC), Barcelona, Spain
[3] Experimental Trauma Surgery, Justus-Liebig-University of Giessen, Germany
[4] Department of Trauma, Hand, and Reconstructive Surgery, University Hospital of Giessen, Germany
[5] School of Biomedical Engineering, McMaster University, Hamilton, ON, Canada

[*] Corresponding authors:

Joseph Deering	Prof. Kathryn Grandfield
McMaster University	McMaster University
1280 Main Street West	1280 Main Street West
Hamilton, ON, L8S 4L7	Hamilton, ON, L8S 4L7
Canada	Canada
Email: deeringj@mcmaster.ca	Email: kgrandfield@mcmaster.ca

S.1   Compliance Corrections for Uniaxial Compression Experiment

Subscripts
exp: Experimentally measured stress or strain values;
m: Stress or strain values induced from machine compliance;
s: Corrected stress or strain values of the specimen

S.1.1 Determine Machine Compliance/Stiffness

In the uniaxial compression test of this study, a cylindrical specimen with a known cross-sectional area A and height H were compressed between two platens that were spring loaded within a screw driven universal mechanical tester. During the compression test, the load cell as well as the screw driven system would introduce additional displacement values d_M that should be subtracted out to obtain the correct measure of the stress-strain values of the specimen. This subsection will determine the calculation of machine compliance during the compression test.

We shall first define the machine compliance to be $C_m \equiv \frac{d_m}{P_m}$; where P_M is the reaction load experienced by the machine and d_M is the additional displacement caused by the flex of the

machine. Since the specimen was sandwiched under the testing machine, iso-force condition is applied during the uniaxial compression test, i.e:

(Eqn. 1a) $P_{exp} = P_m = P_s = P$;

(Eqn. 1b) $d_{exp} = d_m + d_s$;

The second expressions can be rewritten by multiplying $1/H$ into Eqn. 1b:

(Eqn. 2) $\varepsilon_{exp} = \frac{d_m}{H} + \varepsilon_s$;

Where ε_{exp} is the experimentally measured compressive strain and ε_S is compressive strain contributed from the specimen.

Considering that the specimen had a uniform cross-sectional area A, Eqn. 2 can be rewritten by multiplying $1/\sigma = A/P$ to both sides:

(Eqn. 3) $\frac{\varepsilon_{exp}}{\sigma} = \frac{AC_m}{H} + \frac{\varepsilon_s}{\sigma}$

For deformation within the elastic region, the machine stiffness expression $\frac{H}{AC_m}$ can be determined by:

(Eqn. 4) $\frac{H}{AC_m} = \left(\frac{1}{E_{exp}} - \frac{1}{E_s} \right)^{-1}$

This equation was applied to the experimental data, where E_{exp} is an iteratively measured modulus of unloading in the solid cylinder and E_s remains the Young's modulus of a full-density specimen of 304L stainless steel (i.e. $E_s = 200$ GPa).

A calibration compression test has been performed on a fully dense specimen. Curve-fitting showed the experimental measured Young's modulus of the full-density 304L stainless steel has a E_{exp} of 9.20 GPa; machine stiffness expression $\frac{H}{AC_m}$ is about 9.64 GPa.

S.1.2 Determine Machine Compliance/Stiffness

After the machine compliance has been determined using the aforementioned calibration test, the Young's modulus of the cellular specimen (E_s) can then be determined by first performing a separate uniaxial compression test to measure the E_{exp} and then solving for E_s by rearranging Eq. 4.

(Eqn. 5) $E_s = \left(\frac{1}{E_{exp}} - \frac{AC_m}{H} \right)^{-1}$

The compression test result of the porous cellular specimen yields a $E_s = 17.4$ GPa according to Eq. 5.

S.2 Natural Frequency of the Implant

Resonance excitation of the porous scaffold results in a rather broad peak at the natural frequency in the clamped condition. Figure S.1 shows the breadth of the peak in the frequency-response curve. Systemic changes resulting in minor deviations of the input frequency can still induce off-peak resonance of the scaffold, but higher than in purely stiffness-controlled or mass-controlled excitation.
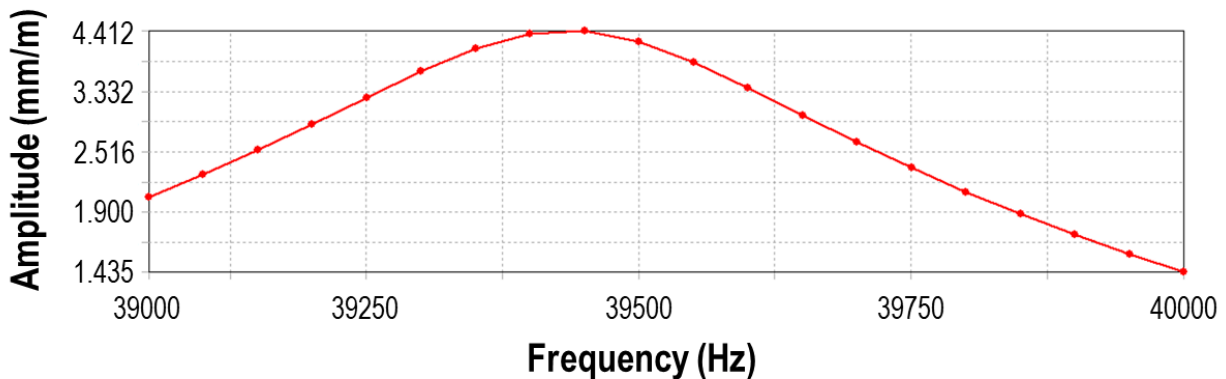

Figure S.1: Frequency-response curve at the natural frequency of the porous stainless steel scaffold. The breadth of the peak allows for off-peak resonant excitation of the scaffold in the damping-controlled region.

S.3 Supplemental Video Captions

Video S1: Mechanical compression of the porous scaffold loaded to 5.5 kN at a strain rate of 0.8 mm/min. Frames are recorded every 5 s.

Video S2: Simulated compression of the porous scaffold in its entirety. Deformation is highest at the top surface.

Video S3: Simulated compression of the porous scaffold in cross-section. Deformation appears uniform through the cross-section.